ACS OMEGA

http://pubs.acs.org/journal/acsodf

Article

ES-MION-Based Dual-Modality PET/MRI Probes for Acidic Tumor Microenvironment Imaging

Xiuyan Wei,[‖] Haitao Zhao,[‖] Gang Huang, Jianhua Liu,* Weina He,* and Qingqing Huang*

Cite This: *ACS Omega* 2022, 7, 3442−3451

Read Online

ACCESS | Metrics & More | Article Recommendations | Supporting Information

ABSTRACT: Among all characteristics of the tumor microenvironment (TME), which are caused by abnormal proliferation of solid tumors, extracellular acidity is an important indicator for malignancy grading. pH-low insertion peptides (pHLIPs) are adopted to discern the acidic TME. To date, different imaging agents including fluorescent, positron emission tomography (PET), single photon emission computed tomography (SPECT), and magnetic resonance (MR) contrast agents with pHLIPs to target the acidic TME have been used to image various tumor models successfully. In this article, a PET/MRI dual-modality probe, based on extremely small magnetic iron oxide nanoparticles (ES-MIONs) with pHLIPs as a targeting unit, was proposed for the first time. In the phantom study, the probe showed relatively high r_1 relaxivity (r_1 = 1.03 mM^{-1} s^{-1}), indicating that it could be used as a T_1-weighted MR contrast agent. The ^{68}Ga-radiolabeled probe was further studied in vitro and in vivo to evaluate pHLIP targeting efficacy and feasibility for PET/MRI. PET with intratumoral injection and T_1-weighted MRI with intravenous injection both showed pHLIP-specific delivery of the probe. Therefore, we successfully designed and developed a radiolabeled ES-MION-based dual-modality PET/MRI agent to target the acidic tumor microenvironment. Although the accumulation of the probe in tumors with intravenous injection was not high enough to exhibit signals in the PET imaging study, our study still provides further insights into the ES-MION-based PET/MRI strategy.

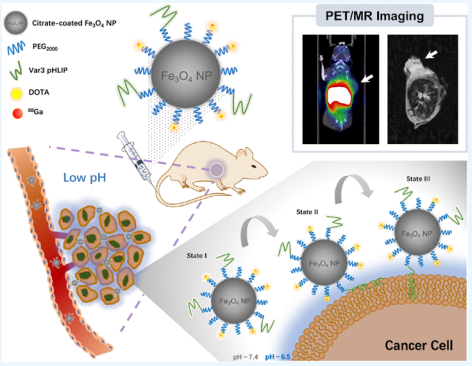

1. INTRODUCTION

Abnormal nutritional requirements and metabolic characteristics of rapid proliferation of solid tumors form a heterogeneous and complex tumor microenvironment (TME). Among all of the features of the TME, the acidic extracellular microenvironment is a common one of malignant tumors.[1] According to the Warburg effect, tumorigenic cells have defective mitochondria and most prefer anaerobic glycolysis even under aerobic conditions. To maintain neutral intracellular pH, the accumulated lactate and H^+ ions generated by upregulated anaerobic glycolysis are released into the extracellular matrix, leading to an acidic extracellular microenvironment.[2] Moreover, some in vitro studies indicated that hypoxia and H^+ ions may further aggravate the accumulation of H^+ ions, resulting in a more acidic microenvironment,[3] which may promote local invasion and obscure immune surveillance of tumor cells by increasing protease activity. Therefore, the acidity of the tumor microenvironment is an important indicator to evaluate the malignant grade of tumor cells.

The acidity of the tumor microenvironment can be recognized by pH-low insertion peptides (pHLIPs). pHLIPs are a family of soluble peptides with 36 amino acid residues, in which lysine residues are partially protonated in the acidic extracellular matrix to form a stable transmembrane α-helix structure allowing pHLIPs to be inserted into the cell membrane.[4] Furthermore, the mildly alkaline (pH 7.4 ± 0.2) intracellular matrix caused by the increased H^+ ion extrusion has a positive impact on the effectiveness of pHLIPs as an imaging agent.[5] Moreover, pHLIPs have been proved to be completely nontoxic and nonimmunogenic, making them an ideal sensing unit for the acidic TME.[6] To identify optimal sequences for in vivo usage, a series of pHLIP variants were studied,[7] among which variant 3 (Var3) appeared to exhibit the most desirable insertion properties.[8,9] The (variant) pHLIP-conjugated probes have been reported to exhibit promising targeting capabilities in various pathological models.[10] Recently, Crawford et al. investigated the tumor-targeting capability and imaging efficacy of the pHLIP-ICG probe in fluorescence-guided surgery.[11] The probe represented a high accuracy of targeting in several murine and human tumor models with a multi-hour circulating half-life, which made it an efficient probe for surgical resection. Demin et al. designed novel organosilicon magnetic nanoparticles, which

Received: October 17, 2021
Accepted: December 31, 2021
Published: January 18, 2022

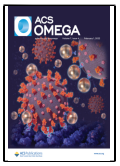

© 2022 The Authors. Published by American Chemical Society

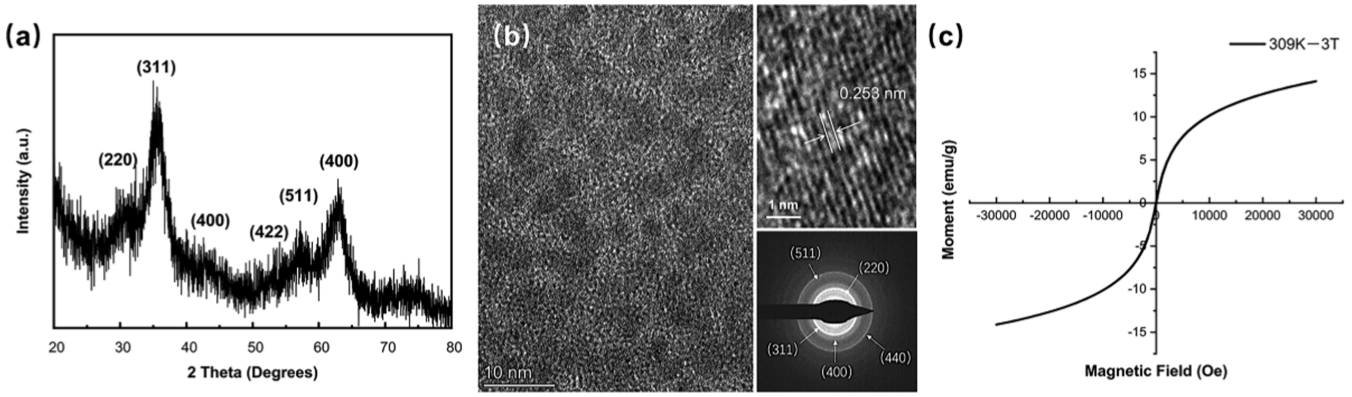

Figure 1. (a) XRD pattern, (b) TEM images, and (c) hysteresis loop of citrate-stabilized Fe_3O_4 NPs.

were covered by poly(ethylene glycol) (PEG) and modified with pHLIPs.[12] The resulting probe was evaluated for its accumulation in 4T1 tumor-bearing BALB/c mice. In the MRI study, pHLIP-modified magnetic nanoparticles demonstrated reliable, safe, and efficient accumulation after intravenous administration. Furthermore, a pHLIP-based imaging agent ([^{18}F]AlF-cysVar3 pHLIP, NCT04054986) is in Phase I clinical trial to be evaluated as a new diagnostic agent.[13]

Among all of the aforementioned studies of pHLIP-related probes, positron emission tomography (PET) probes showed the highest tissue penetration. Although PET could reveal the functional information of lesions with high sensitivity, it hardly provides any anatomical information.[14] By complementing with the advantages of different imaging modalities, multimodal imaging is helpful for the quantitative analysis of the composite target volume of tumors. Thus, it is becoming an indispensable part of biomedical research and clinical diagnostics.[15−18] Among all of the multimodal imaging strategies, the high resolution of magnetic resonance imaging (MRI) can potentially evaluate the heterogeneity of tumor acidity, while positron emission tomography (PET) has superior sensitivity relative to MRI.[19] Thus, it is of great significance to develop PET/MRI combined probes for detecting hypermetabolic lesions in cancer diagnosis.[20]

With the prosperity of nanotechnology, integration of imaging modalities within one nanomedicines system has been attempted to achieve the accurate diagnosis,[21−23] among which the nanoparticle-based dual-modality PET/MRI agent is attractive.[24] The physicochemical properties of nanoparticles, such as inherent optical/magnetic properties, small particle size, large surface area, and designable surface coating, are beneficial for them to aggregate in tumors and circulate in vivo for a long time.[25,26] Among all of the studied nanomaterials, magnetic iron oxide nanomaterials (MIONs) were approved by the US Food and Drug Administration (FDA) in 2009 and have been applied in clinical diagnostic and treatment since then.[27] Due to their tunable magnetism and facile conjugation with targeting ligands, MION-based probes are considered as a kind of ideal MRI contrast agent.[28]

By changing the corresponding relaxivities with nearby water protons, MIONs can provide either positive contrast in T_1-weighted (shorten spin−lattice relaxation) images or negative contrast in T_2-weighted (decrease transverse relaxation) images.[29] The development of MION-based T_2-weighted contrast agents (>10 nm) has largely been ceased based on the following facts: (1) dark images are difficult to be distinguished from those of some pathogenic conditions (e.g., hemorrhage, calcification, metal deposits, etc.) and (2) the resolution of images is reduced by a large-magnetic-moment-induced susceptibility artifact. On the contrary, exceedingly small magnetic iron oxide nanoparticles (ES-MIONs, <5 nm) can be used as T_1 contrast agents for MRI. ES-MIONs exhibit high magnetization with an extremely high r_1 relaxation rate and a low r_2/r_1 ratio under clinical field strength.[30] Compared with the clinic commonly used gadolinium complex for T_1-weighted MRI, ES-MIONs can achieve MR imaging with comparable high resolution with less toxicity and lower cost.[31] ES-MIONs are more capable of avoiding rapid renal clearance than small molecules and degrade faster compared to larger MIONs in reticuloendothelial system (RES) organs by retarding the uptake. Furthermore, ES-MIONs are proved to permeate farther in the tumor tissue with better intratumoral distribution.[32] Hence, ES-MIONs are expected to be an excellent vector for multimodal PET/MRI imaging.[33]

Herein, we reported a multifunctional MION-based probe functionalized by pHLIPs to target the acidic tumor microenvironment for PET/MRI dual-modality imaging of tumors. Because of the enhanced permeability and retention (EPR) effect, the uptake and distribution of nanomaterials in tumors are believed to be heterogeneous.[34,35] In this study, by integrating pHLIPs, the nanoprobes are designed to be inserted into cell membranes for enrichment after sensing the acidic tumor microenvironment, which may reduce the heterogeneous uptake caused by the EPR effect. This design provides a new strategy for the development of nanomaterials as imaging agents.

In this article, ES-MIONs were synthesized by the solvothermal method with the surface functionalized by Var3 pHLIPs. As evaluated in cellular and in vivo studies, the probe was found to be efficient to target the tumor microenvironment and visualize tumors via T_1-weighted positive MR imaging. Although the results of PET imaging in vivo with intravenous injection were not satisfactory because of the imperfect physicochemical properties of the probe and/or instability of the ^{68}Ga chelate, our work still provided a new strategy for evaluation and diagnosis of malignant tumors using ES-MION-based dual-modality imaging probes.

2. RESULTS AND DISCUSSION

2.1. Synthesis and Properties of Fe_3O_4-PEG-DOTA/pHLIP NPs. Citrate-stabilized Fe_3O_4 nanoparticles (Fe_3O_4 NPs) were synthesized *via* a solvothermal process. The characteristic peaks at 2θ = 30.4, 35.9, 43.2, 54.1, 57.2, and 63.1° on the X-ray diffraction (XRD) pattern corresponded to

https://doi.org/10.1021/acsomega.1c05815
ACS Omega 2022, 7, 3442−3451

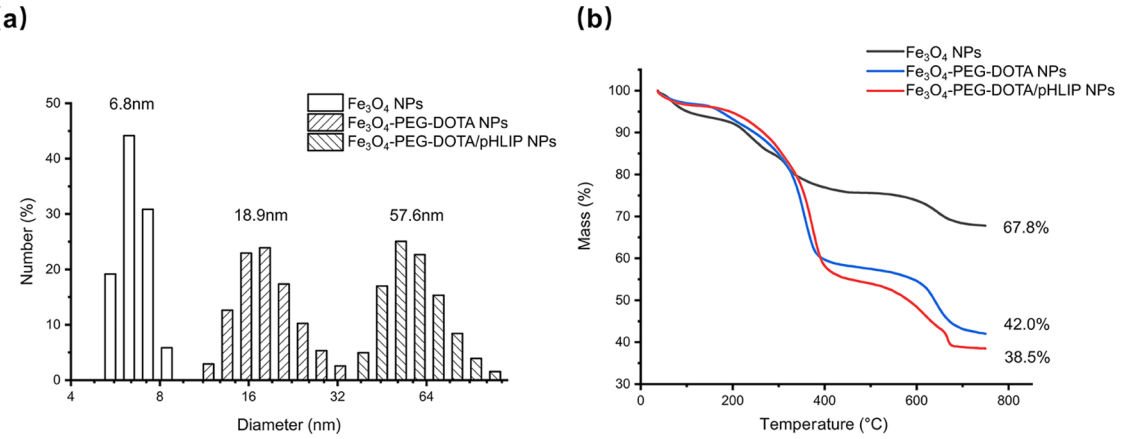

Figure 2. (a) DLS measurements and (b) TGA curves of citrate-stabilized Fe_3O_4 NPs, Fe_3O_4-PEG-DOTA NPs, and Fe_3O_4-PEG-DOTA/pHLIP NPs.

the diffraction planes of (220), (311), (400), (422), (511), and (440), respectively, indicating the standard cubic inverse spinel structure of magnetite Fe_3O_4 NPs (Fe_3O_4, ICDD: 19-0629; Figure 1a). The high-resolution transmission electron microscopy (HR-TEM) results also demonstrated a d-spacing value of 0.253 nm corresponding to the (311) lattice fringes of Fe_3O_4 NPs (Figure 1b). These analyses are consistent with the selected area electron diffraction (SAED) patterns (Figure 1b). In the observation of the hysteresis loop of the nanoparticles, the superparamagnetic properties of these Fe_3O_4 NPs were revealed with negligible remanence and coercive force at 309 K (Figure 1c). In addition, the hysteresis loops measured at 298 and 309 K showed a slight difference, suggesting that Fe_3O_4 NPs could maintain superparamagnetic properties in the normal application temperature range (Figure S2).

Then, pristine citrate-stabilized Fe_3O_4 NPs were modified with NH_2-PEG-pHLIP/NH_2-PEG-DOTA or NH_2-PEG-DOTA. The structures of NH_2-PEG-pHLIP and NH_2-PEG-DOTA were characterized by Fourier transform infrared (FTIR) spectra (Figure S3). For NH_2-PEG-pHLIP, the characteristic vibrations existed at 1640 cm^{-1} ($\nu_{C=O\ imide}$) but disappeared at 2600 cm^{-1} (−SH groups of pHLIP). For NH_2-PEG-DOTA, the combined signals at 1635 cm^{-1} ($\nu_{C=O}$ of the amide bond) and 1350 cm^{-1} (ν_{C-N}) suggested the existence of DOTA in the product. The ^1H NMR signals confirmed the structures of NH_2-PEG-pHLIP and NH_2-PEG-DOTA (Figure S4). For NH_2-PEG-pHLIP, ^1H NMR (400 MHz, $CDCl_3$), δ (ppm): 7.26 (s, 24H), 3.63 (s, 5H), 1.56 (s, 70H), 1.25 (s, 2H). For NH_2-PEG-DOTA, ^1H NMR (400 MHz, $CDCl_3$), δ (ppm): 7.26 (s, 3H), 3.65 (s, 29H), 1.83 (s, 2H), 1.25 (s, 4H).

The functionalization of Fe_3O_4 NPs was proved to be successful by measuring the hydrodynamics diameter and ζ-potential. The average hydrodynamics diameter of citrate-stabilized Fe_3O_4 NPs was found to be 6.8 nm, as revealed by dynamic light scattering (DLS) detection (Figure 2a). Fe_3O_4-PEG-DOTA/pHLIP NPs were obtained by covalently bonding NH_2-PEG with citrate-covered Fe_3O_4 NPs via EDC/NHS coupling chemistry. With functionalization, the hydrodynamic diameters of Fe_3O_4-PEG-DOTA NPs and Fe_3O_4-PEG-DOTA/pHLIP NPs increased to 18.9 and 57.6 nm, respectively (Figure 2a). At pH 6.8, the ζ-potential of Fe_3O_4-PEG-DOTA NPs was −18.1 mV, while that of Fe_3O_4-PEG-DOTA/pHLIP NPs was −27.3 mV compared with the unfunctionalized citrate-stabilized Fe_3O_4 NPs, of which the ζ-potential was about −35.2 mV. With the process of surface grafting, the hydrodynamic size and ζ-potential of the nanoparticles changed dramatically, which proved the successful grafting of pHLIPs and DOTA onto the surface of Fe_3O_4 NPs

The structure and size of Fe_3O_4 NPs were characterized by HR-TEM. The results indicated that the citrate-stabilized Fe_3O_4 NPs were spherical and well dispersed, exhibiting an average diameter of 3.09 nm with a narrow size distribution (Figures 1b and S5). According to the HR-TEM results, Fe_3O_4-PEG-DOTA/pHLIP NPs and Fe_3O_4-PEG-DOTA NPs barely showed differences compared with the unfunctionalized citrate-stabilized Fe_3O_4 NPs (Figure S6), which was caused by the collapse of the molecular chain in the PEG-DOTA/pHLIP shell and the low TEM contrast of macromolecules. Nevertheless, based on the TEM results, functionalized nanoparticles still maintain a monodisperse state, suggesting necessary hydrophilicity for tumor imaging. SAED patterns indicated that the crystal structure was not affected by surface modification, suggesting that the surface-modified nanoparticles still maintain superb superparamagnetism (Figure S6).

The amount of the organic shell around Fe_3O_4 NPs was evaluated by thermogravimetric analysis (TGA). When heating up to 750 °C, the citrate-stabilized Fe_3O_4 NPs showed a weight loss of 32.2% due to the presence of citrate on the particle surface, while the weight losses of Fe_3O_4-PEG-DOTA NPs and Fe_3O_4-PEG-DOTA/pHLIP NPs were 58.0 and 61.5%, respectively (Figure 2b). By subtracting the weight loss of Fe_3O_4 NPs (32.2%), the loading percentages of PEG-DOTA (for nontargeted particles) and PEG-DOTA/pHLIP (for targeted particles) on the surface of Fe_3O_4 NPs are 25.8 and 29.3%, respectively. Through calculation, each Fe_3O_4-PEG-DOTA NP is grafted with an average of 5.3 PEG molecules (with a ratio of 1:1 for $-NH_2$ and −DOTA as end groups). Each Fe_3O_4-PEG-DOTA/pHLIP NP is grafted with an average of 5.2 PEG molecules (with a ratio of 2:2:1 for $-NH_2$, −DOTA, and −pHLIP as end groups). The high grafting percentage was contributed by the large specific surface area of nanoparticles with an ultrasmall size.[36]

2.2. Phantom Study. The phantom study was conducted to investigate the feasibility of Fe_3O_4-PEG-DOTA/pHLIP NPs as T_1 MR imaging contrast agents at a room temperature range of 32−34 °C and pH 6.8. Although there are limited

https://doi.org/10.1021/acsomega.1c05815
ACS Omega 2022, 7, 3442−3451

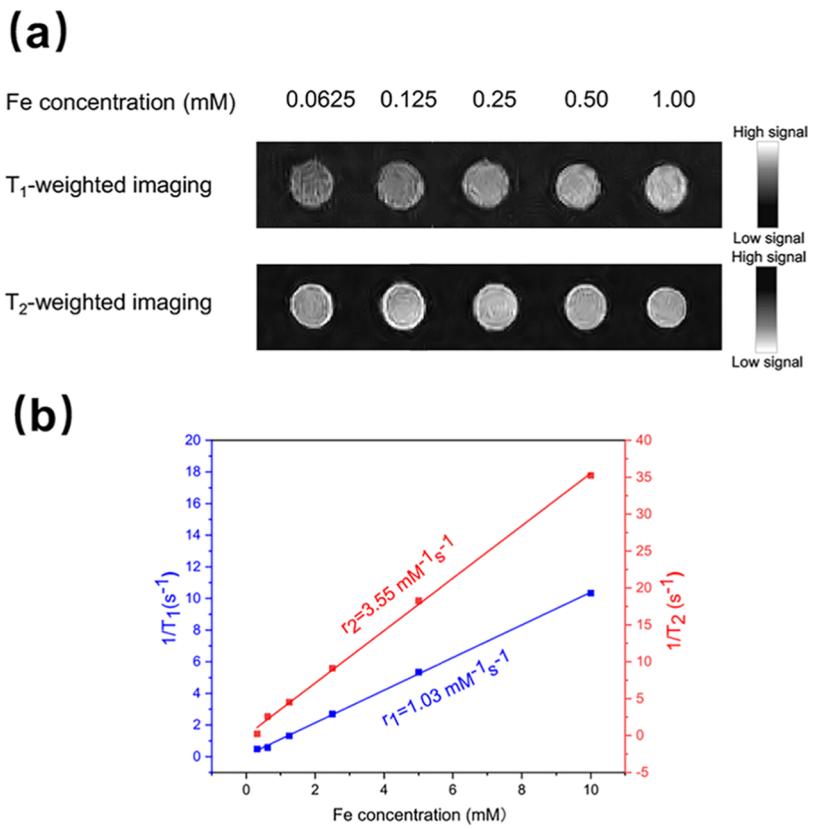

Figure 3. (a) Phantom image acquired from T_1-weighted and T_2-weighted MRI scans for Fe_3O_4-PEG-DOTA/pHLIP NPs at different Fe concentrations at a room temperature range of 32−34 °C and pH 6.8. (b) Plot of the relaxation rates of Fe_3O_4-PEG-DOTA/pHLIP NPs as a function of Fe concentration at a room temperature range of 32−34 °C and pH 6.8.

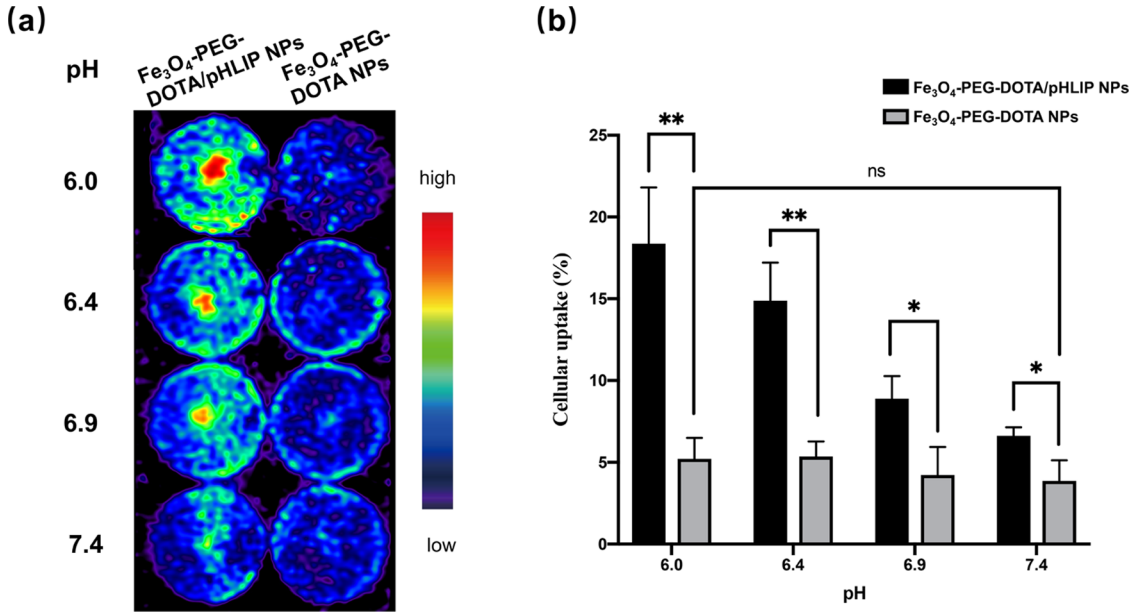

Figure 4. (a) PET images and (b) graph of the in vitro cell binding of Fe_3O_4-PEG-[^{68}Ga]DOTA/pHLIP NPs and Fe_3O_4-PEG-[^{68}Ga]DOTA NPs of 4T1 cells in pH 6.0, 6.4, 6.9, and 7.4. *P < 0.1 and **P < 0.01. ns: not statistically significant.

differences between the physiological environment and the in vitro experimental conditions, the r_1 and r_2 test results obtained in the phantom study still provide a considerable reference. The imaging enhancement performance of the MRI contrast agent was then evaluated using in vivo MR imaging. The signal contrast enhancement effect appeared in the T_1-weighted MR images of Fe_3O_4-PEG-DOTA/pHLIP NPs, as represented in Figure 3a. It was obvious that both Fe_3O_4-PEG-DOTA/pHLIP NPs and Fe_3O_4-PEG-DOTA NPs (Figure S7) displayed increased MR signal intensity with Fe concentrations ranging from 0.06 to 1.00 mM dependently. Actually, for nanoparticles functionalized with pHLIPs, T_1-weighted MRI

https://doi.org/10.1021/acsomega.1c05815
ACS Omega 2022, 7, 3442−3451

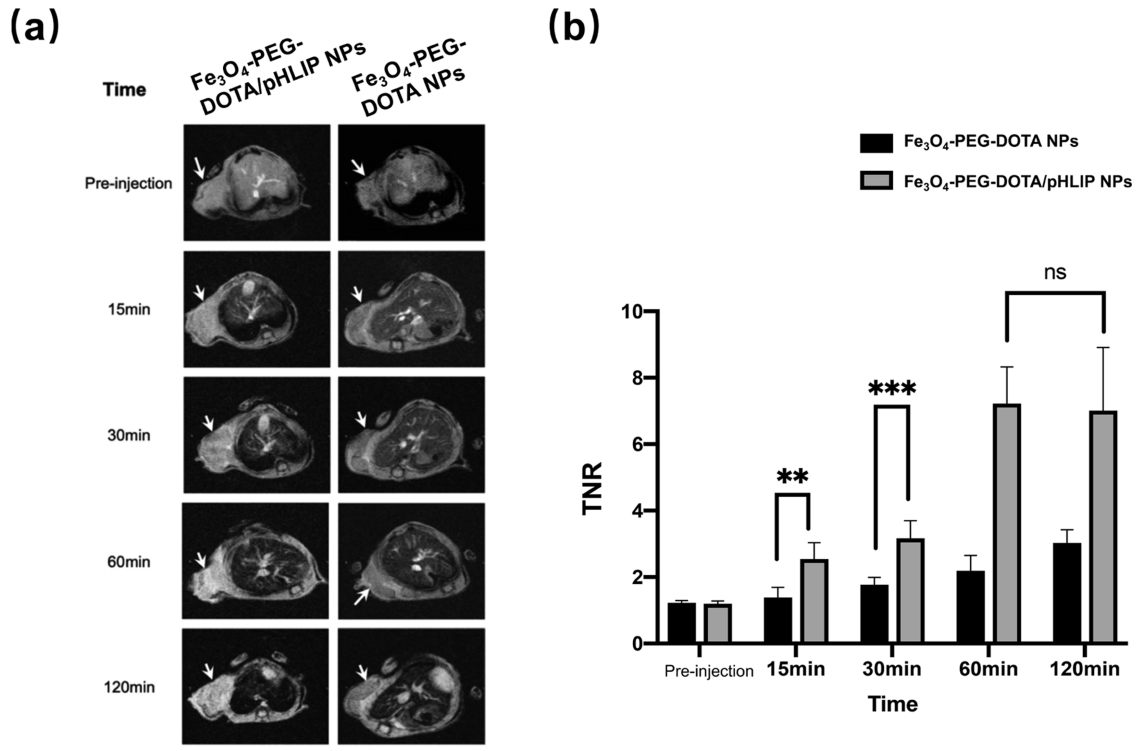

Figure 5. (a) In vivo T_1-weighted MR images and (b) quantification of TNR of 4T1 tumor-bearing mice (slice orientation: axial) after intravenous injection of Fe_3O_4-PEG-DOTA/pHLIP NPs or Fe_3O_4-PEG-DOTA NPs. $^{**}P < 0.01$ and $^{***}P < 0.001$. ns: not statistically significant.

signal intensity exhibited a positive linear correlation with the Fe concentration in a wide range of 0.31−10.00 mM (Figure S8). In contrast, T_1-weighted MRI signal intensity began to decrease as the Fe concentration increased more than 1.25 mM for nanoparticles without pHLIP modification due to the obstructing caused by T_2-weighted imaging. By plotting the relaxation rate as a function of Fe concentration, the r_1 and r_2 of Fe_3O_4-PEG-DOTA/pHLIP NPs were calculated to be 1.03 and 3.55 mM^{-1} s^{-1}, respectively (Figure 3b). With a low r_2/r_1 ratio of 3.45, Fe_3O_4-PEG-DOTA/pHLIP NPs represented optimal properties for efficient T_1 contrast. MR imaging of the analogous nanoparticles used for the relaxivity measurements confirmed the strong T_1 effect and the low T_2 effect.[30] Therefore, it is well established that Fe_3O_4-PEG-DOTA/pHLIP NPs can be used as a kind of promising T_1-weighted contrast agent.

2.3. Cytocompatibility Assay. The cytotoxicity of the probes was evaluated in vitro with 4T1 cells. After treating with Fe_3O_4-PEG-DOTA/pHLIP NPs or Fe_3O_4-PEG-DOTA NPs (Fe concentration: 2.5−300 μg/mL) for 24 h, 4T1 cells all exhibited a high survival rate (higher than 80%, Figure S9), suggesting the good biocompatibility of both kinds of nanoparticles.

2.4. Cell Binding Assay. To investigate the tumor-targeting efficacy of the probes, cell binding was measured after incubating ^{68}Ga-radiolabeled Fe_3O_4-PEG-DOTA/pHLIP NPs or Fe_3O_4-PEG-DOTA NPs with 4T1 cells. The cell binding rate of Fe_3O_4-PEG-[^{68}Ga]DOTA/pHLIP NPs, which represented strong pH dependence, was significantly higher than that of Fe_3O_4-PEG-[^{68}Ga]DOTA NPs (Figure 4a and Table S1). It is worth noting that the signal strength is slightly higher at pH 6.9 than that at pH 6.4 for Fe_3O_4-PEG-[^{68}Ga]DOTA/pHLIP NPs, probably due to the fact that there are pHLIPs bound to the cell membrane in the form of state II at neutral pH (~6.9).[4] Moreover, no significant difference in cell binding was found when 4T1 cells were treated with Fe_3O_4-PEG-[^{68}Ga]DOTA NPs under different pH conditions. Additionally, the binding percent of 4T1 cells with Fe_3O_4-PEG-[^{68}Ga]DOTA/pHLIP NPs at pH 6.0 reached 18.36 ± 3.45%, which was significantly higher than that at pH 7.4 (6.61 ± 0.53%) and also higher than the binding percentage of 4T1 cells with Fe_3O_4-PEG-[^{68}Ga]DOTA NPs (3.86 ± 1.26 to 5.21 ± 1.28%; Figure 4b). These results indicated that Fe_3O_4-PEG-[^{68}Ga]DOTA/pHLIP NPs could target the acidic microenvironment with a positive correlation between extracellular acidity and targeting efficacy.

2.5. In Vivo MR Imaging and PET Imaging. The potency of Fe_3O_4-PEG-DOTA/pHLIP NPs used as tumor-targeting nanoprobes for in vivo MR imaging with intravenous injection was evaluated. Fe_3O_4-PEG-DOTA NPs were also studied in the same model as control. In vivo T_1-weighted fast spin-echo MRI was performed on mice bearing 4T1 tumors. The results confirmed the strong T1 effect observed in the former in vitro studies. The signal intensity was enhanced after the intravenous injection of both nanoprobes (Figure 5a). TNR (tumor-to-normal tissue ratios) was used to quantify the effect of two probes on the difference in targeting between tumor and normal tissue. It was obvious that Fe_3O_4-PEG-DOTA/pHLIP NPs began to accumulate within 15 min after injection, resulting in stronger signals. Meanwhile, imaging with Fe_3O_4-PEG-DOTA NPs maintained weaker signals throughout the whole experiment (Figure 5b). Hence, Fe_3O_4-PEG-DOTA/pHLIP NPs were proved to be a kind of T_1-weighted imaging contrast agent, which exhibits a better MR imaging effect. All in all, the MR imaging results and MR SNR data revealed that the nanoprobes functionalized with pHLIPs were better tumor-targeting nanoprobes for in vivo T_1-weighted positive MR imaging.

https://doi.org/10.1021/acsomega.1c05815
ACS Omega 2022, 7, 3442−3451

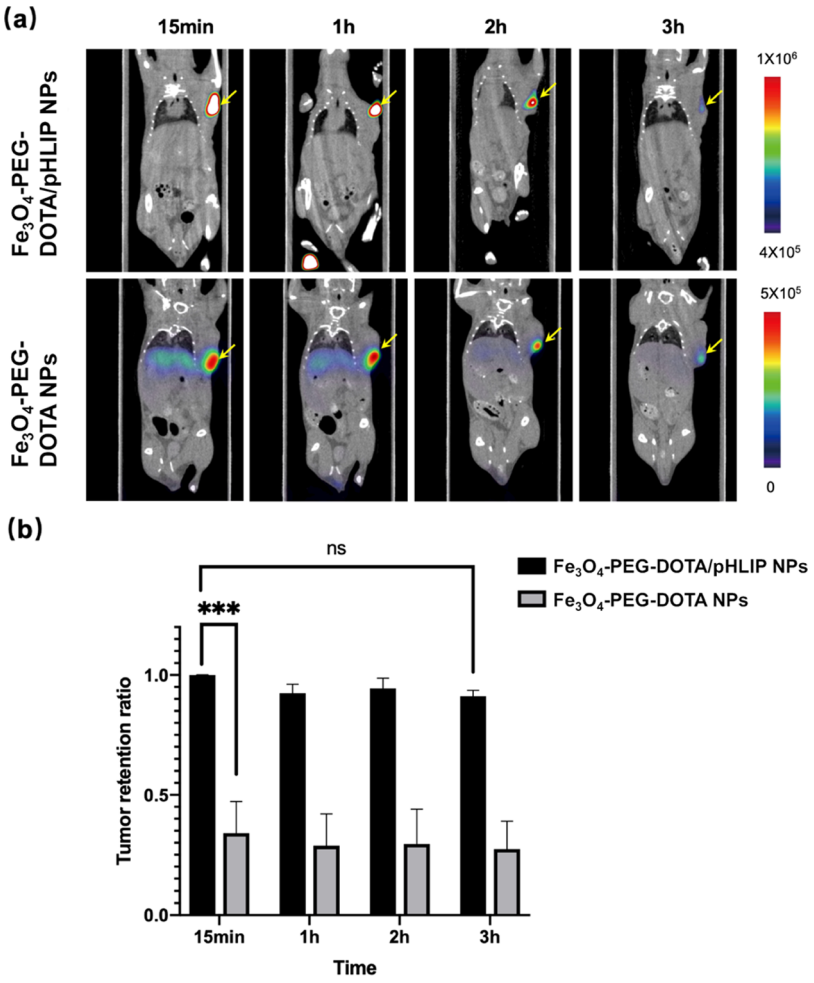

Figure 6. PET/CT of 4T1 tumor-bearing mice after intratumoral injection of Fe_3O_4-PEG-[^{68}Ga]DOTA/pHLIP NPs or Fe_3O_4-PEG-[^{68}Ga]DOTA NPs. (a) Images reveal the signal changes in the whole body and (b) probe retention rate in the tumor region by the max signal of the tumor.

The in vivo tumor retention of Fe_3O_4-PEG-[^{68}Ga]DOTA/pHLIP and Fe_3O_4-PEG-[^{68}Ga]DOTA nanoprobes in 4T1 tumor-bearing mice were evaluated by micro-PET/CT. The results of intratumoral injection are represented in Figure 6a. Compared with the Fe_3O_4-PEG-[^{68}Ga]DOTA nanoprobe, the pHLIP-conjugated nanoprobe showed a longer retention time and a higher retention ratio within tumors, while its elimination rate in normal tissues and/or the blood was slow. The result revealed that the Fe_3O_4-PEG-[^{68}Ga]DOTA/pHLIP nanoprobe could remain in tumor tissue for at least 3 h (Figure 6b). Meanwhile, the Fe_3O_4-PEG-[^{68}Ga]DOTA nanoprobe showed noticeable accumulation in the liver and the spleen over time. These results suggested that pHLIP played a significant role in targeting the tumor acidic microenvironment.

Unfortunately, in vivo PET imaging with intravenous injection of both nanoprobes studied showed slight uptake in the tumor area (Figure S10). On the other hand, high signals appeared in the liver and the spleen.

The pHLIP-conjugated nanoparticles obviously exhibited enhanced signals on MR imaging but did not show high uptake in the tumor area on PET imaging in vivo. The reasons may lie in (1) the imperfect physicochemical property of the nanoprobe and (2) the instability of the ^{68}Ga chelate in the presence of serum proteins. The imperfect physicochemical property, which mainly refers to the poor hydrophilicity and electronegativity of the nanoprobe, could lead to the low tumor-targeting accompanied by short blood circulation. Limited by the radiolabeling protocol, the amount of nanoprobes for PET is relatively lower than that of MRI, which means that the tumor-targeting ability of the nanoprobe needs to be improved, especially for PET imaging.

However, attempts to improve the potency of nanoprobes by grafting more pHLIPs onto MIONs were proved to be unprofitable. Because nanoprobes grafted with more pHLIPs exhibited poor hydrophilicity, which could not be carried out for further radiolabeling. To overcome this limitation, it will be helpful to aggravate the crowdedness of the PEG shell (can be quantified and characterized by R_F/D, where R_F is the Flory radius, which directly depends on the PEG molecular weight and D is the distance between two neighboring PEG anchors, which is inversely correlated to the grafting density)[37] by increasing the grafting density of PEG or the coating thickness. Compared with increasing the grafting density, it seems to be more effective to increase the chain length of PEG on the surface of MIONs.[38]

To solve the poor uptake in the tumor area on PET imaging, some optimizations were recommended: (1) Improve the hydrophilicity of the nanoprobes. Thus, the circulation time is prolonged, contributing to the higher accumulation in tumor tissue. (2) Decrease the electronegativity of the nanoprobes. With the increase of the grafting amount of electrically neutral

https://doi.org/10.1021/acsomega.1c05815
ACS Omega 2022, 7, 3442−3451

PEG, the surface potential of NPs tends to be more neutral, which will reduce the uptake of nanoprobes by the RES system.[39] (3) Using multiarmed PEG is also an alternative strategy.[40] The multiarmed PEG strategy can not only increase the grafting amount of pHLIPs to accelerate tumor targeting but also maintain the adaptable hydrophilicity of the probe at the same time. (4) Besides, bifunctional chelates that can be efficiently radiolabeled with Ga to yield complexes with better in vivo stability are needed, such as NOTA (1,4,7-triazacyclononane-1,4,7-triacetic acid).[41]

3. CONCLUSIONS

In summary, citrate-stabilized ES-MIONs were synthesized via a solvothermal procedure. With the surface functionalization of NPs with pHLIPs and a radioactive metal chelator (DOTA), Fe_3O_4-PEG-DOTA/pHLIP NPs were prepared. The characterization of the nanoparticles revealed exceeding small size, excellent stability, superparamagnetic property, and high biocompatibility. In the in vitro study, it was confirmed that nanoparticles studied were potent MR T_1 imaging contrast agents, and the radiolabeled nanoparticles were capable of targeting the acidic extracellular microenvironment via PET imaging. From the in vivo MRI study for 4T1 tumor-bearing mice with intravenous injection, the nanoparticles were verified to act as effective contrast agents with tumor-specific contrast enhancement effects. Moreover, PET imaging of 4T1 tumor-bearing mice with intratumoral injection exhibited prolonged retention in tumor regions. These results fully illustrated pHLIPs playing an important role in targeting and delivering the probes to tumors. Unexpectedly, in vivo PET imaging study with intravenous injection failed to visualize the tumor evidently, which may be caused by slow tumor targeting accompanied by short blood circulation and/or instability of the ^{68}Ga chelate. In summary, we synthesized pHLIP-conjugated MIONs as a kind of dual-modality imaging probe, which can not only target the acidic tumor microenvironment actively but also visualize tumors with MRI in vivo. Although the study of PET imaging with intravenous injection was unsatisfactory, our study provided certain significance for the ES-MION-based PET/MRI strategy in which ES-MION-based dual-modality imaging probes are used for evaluation and diagnosis of malignant tumors.

4. METHODOLOGY AND MATERIALS

4.1. Materials. All chemicals were of analytical grade from commercial sources and used without further purification. Ferrous chloride tetrahydrate ($FeCl_3{\cdot}6H_2O$, 97%), sodium acetate, sodium citrate, dimethyl sulfoxide (DMSO), *N*,*N*-dimethylformamide (DMF), 1-ethyl-3-(3-dimethylaminopropyl) carbodiimide hydrochloride (EDC), and *N*-hydroxysuccinimide (NHS) were purchased from Sigma-Aldrich (St. Louis, MO). Triethylamine, diethylene glycol, and all of the other solvents were purchased from Sinopharm Chemical Reagent Co., Ltd (Shanghai, China). NH_2-PEG_{2000}-Mal, NH_2-PEG_{2000}-Fmoc, and DOTA-NHS were purchased from Xi'an Ruixi Biological Technology Co., Ltd. pHLIP AW-27 (Var3 sequence: ACDDQNPWRAYLDLLFPTDTLLLDLLW) was custom-made from GL Biochem (Shanghai, China). Fetal bovine serum (FBS), penicillin, and streptomycin were purchased from Gibco (Carlsbad, CA). Water used in all experiments was purified using a RephiLe Genie Water System (RephiLe Bioscience, Ltd.) with a resistivity higher than 18 MΩ cm before usage. Regenerated cellulose dialysis membranes (molecular weight cutoff, MWCO = 1000 or 3500) were acquired from Spectrum Labs.

4.2. Synthesis and Modification of Fe_3O_4-PEG-DOTA/pHLIP NPs and Fe_3O_4-PEG-DOTA NPs. *4.2.1. Synthesis of Citrate-Stabilized Fe_3O_4 Nanoparticles.* $FeCl_3{\cdot}6H_2O$ (10 mmol) was dissolved in 100 mL of diethylene glycol under room temperature. Sodium citrate (4 mmol) was added to the above solution, and the resulting mixture was heated to 80 °C to form a homogeneous yellow solution. Subsequently, sodium acetate (40 mmol) was added to the above solution, and then the mixture was transferred to a Teflon-lined stainless steel autoclave and sealed. The autoclave was heated in an oven at 200 °C for 4 h. After cooling down to room temperature, the raw product was purified with ethanol three times by centrifugation (10 000 rpm, 5 min) to remove excess reactants and byproducts. After removing the solvent by rotary evaporation, the Fe_3O_4 NP crystalloid was obtained for further use.

4.2.2. Synthesis of NH_2-PEG-pHLIP. NH_2-PEG-Mal (0.1 mmol) was dissolved in 5 mL of DMSO under vigorous magnetic stirring at 35 °C, followed by the addition of pHLIP (0.2 mmol, dissolved in 2 mL of DMSO). The reaction mixture was stirred for 24 h. The mixture was then purified by dialysis against phosphate-buffered saline (PBS, three times, 2 L) and water (six times, 2 L) for 3 days using a dialysis membrane (RC) with an MWCO of 3.5 kDa. A further lyophilization process was carried out to afford the product NH_2-PEG-pHLIP as a white powder.

4.2.3. Synthesis of NH_2-PEG-DOTA. Fmoc-PEG-NH_2 (0.2 mmol), DOTA-NHS (0.4 mmol), and a catalytic amount of triethylamine (5%) were dissolved in DMF (10 mL). The reaction mixture was magnetically stirred at room temperature for 3 h. Piperidine (2 mL) was then added into the reaction mixture that was kept in the shaking stage for 18 h at 40 °C. The mixture was purified by dialysis against phosphate-buffered saline (PBS, three times, 2 L) and water (six times, 2 L) for 3 days using a dialysis membrane with an MWCO of 1 kDa. A further lyophilization process was carried out to yield the product NH_2-PEG-DOTA as a yellow solid.

4.2.4. Preparation of Fe_3O_4-PEG-DOTA/pHLIP NPs and Fe_3O_4-PEG-DOTA NPs. The mixture of citrate-stabilized Fe_3O_4 NPs (50 mg, 10 mL of DMSO), EDC (320 mg, dissolved in 1 mL of DMSO), and NHS (187 mg, dissolved 1 mL of DMSO) was stirred at room temperature for 3 h. The resulting solution was added dropwise into a DMSO solution (5 mL) of NH_2-PEG-pHLIP (26.1 mg) and NH_2-PEG-DOTA (55.23 mg) under vigorous stirring at room temperature for 3 d. The reaction mixture was purified by magnetic bead adsorption. A further lyophilization process was carried out to afford the product Fe_3O_4-PEG-DOTA/pHLIP NPs as a dark powder. The synthesis process is intuitively shown in figure S1.

Fe_3O_4 NPs were also reacted with NH_2-PEG-DOTA following a similar experimental procedure to obtain Fe_3O_4-PEG-DOTA NPs.

4.3. Cell Lines and the Animal Model. Mouse breast cancer cell line 4T1 was originally obtained from American Type Culture Collection (ATCC) and cultured in a monolayer culture in 1640 culture medium supplemented with 1% penicillin, streptomycin, and 10% fetal bovine serum (v/v) under a humidified atmosphere at 37 °C containing 5% CO_2. The xenografted tumor model was established by subcutaneously injecting 1.5×10^6 cells in 1 mL of phosphate-buffered

https://doi.org/10.1021/acsomega.1c05815
ACS Omega 2022, 7, 3442−3451

saline into the right armpit of 6-week-old female BALB/c mice (Charles River). The mice were used for small-animal PET and MRI studies when the tumor volume reached 100−200 mm^3 (1 week after inoculation). All applicable institutional and/or national guidelines for the care and use of animals have been complied with.

4.4. Characterization. DLS measurements were performed with a Malvern Instruments Zetasizer Nano Series Nano-ZS (Worcestershire, United Kingdom) equipped with a standard 633 nm laser. TEM images and SAED patterns were obtained on a TALOS F200X (Thermo Scientific, Hudson, NH) operated at an accelerating voltage of 200 kV. After embedding Fe_3O_4 nanoparticles with epoxy resin and being sliced, samples for TEM analysis were prepared by loading them on copper grids covered with a lacey carbon support film. To characterize the crystal structure of the products, XRD was performed using a Bruker D8 Advance X-ray diffractometer (BRUKER AXS, Germany) and the scanning range (2θ) was from 20 to 80°. The measurements of field-dependent magnetization (M−H curves) were carried out using a Quantum Design MPMS3 VSM-SQUID magnetometer with a sensitivity of 10^{-8} emu up to a maximum field of 7T. FTIR spectra from KBr disks of the functionalized PEG were obtained on a Thermo fisher Nicolet 6700 Fourier transform spectrometer (Waltham). ^{1}H NMR spectra were collected using a Bruker Avance 400 MHz FT-NMR spectrometer, with $CDCl_3$ as a solvent. TGA was carried out with an SDT Q600 TGA/DSC instrument (TA Instruments), by heating the sample up to 750 °C under a nitrogen flow at a heating rate of 10 °C/min. T_1-weighted imaging and T_1 and T_2 relaxometry were performed by a 0.5T MesoMR23-060V-I (relaxation analysis and imaging) integrated nuclear magnetic imaging analyzer (Shanghai NIUMAG Corporation, Shanghai, China). The samples were diluted in water with the Fe concentration in the range of 0.03−1.00 mM. T_1 and T_2 relaxometry were calculated by linearly fitting the inverse relaxation time as a function of Fe concentration.

4.5. In Vitro Cytotoxicity Study. The cytotoxicities of Fe_3O_4-PEG-DOTA/pHLIP NPs and Fe_3O_4-PEG-DOTA NPs were evaluated by the MTT viability assay. 4T1 cells were inoculated into 96-well plates (Dutscher, France) with a density of 8000 per well in 200 μL of complete culture medium. After adherence, Fe_3O_4-PEG-DOTA/pHLIP NPs or Fe_3O_4-PEG-DOTA NPs at different Fe concentrations (0−300 $\mu g \cdot mL^{-1}$) were added and incubated for 24 h at 37 °C and 5% CO_2. After adding 20 μL of the CCK-8 reagent to each well, incubation was continued for another 1 h in the cell culture incubator. The absorbance (OD) at 450 nm in each well was measured using a PerkinElmer EnSight (PerkinElmer, Shanghai). The mean and standard deviation for the triplicate wells were reported.

4.6. Radiolabeling of Fe_3O_4-PEG-DOTA/pHLIP NPs and Fe_3O_4-PEG-DOTA NPs with ^{68}Ga. ^{68}Ga was eluted from the ^{68}Ge/^{68}Ga generator by 5 mL of 0.1 M HCl, and the second tube of 1 mL of eluent for radiolabeling was used. The ^{68}Ga eluent (370 MBq) was mixed with 150 μL of 1 M NaOAc and Fe_3O_4-PEG-DOTA/pHLIP NPs (100 μg) or Fe_3O_4-PEG-DOTA NPs (100 μg) and heated at 100 °C for 25 min. After cooling, the filtrate was purified using a PD-10 desalting column (GE Healthcare) with phosphate-buffered saline as the mobile phase for subsequent experiments.

4.7. In Vitro Cell Binding Assay. The in vitro binding of Fe_3O_4-PEG-[^{68}Ga]DOTA/pHLIP NPs or Fe_3O_4-PEG-[^{68}Ga]-DOTA NPs to 4T1 cells was analyzed. Approximately 370 kBq of Fe_3O_4-PEG-[^{68}Ga]DOTA/pHLIP NPs or Fe_3O_4-PEG-[^{68}Ga]DOTA NPs were added into 6×10^5 cells in 1.5 mL centrifuge tubes. After incubation at 4 °C for 1 h, the cells were washed three times with ice-cold PBS buffer and collected into radioimmunoassay tubes. All tubes were measured with PerkinElmer counter WIZARD2 to obtain cell-associated radioactivity. The results were expressed as the binding percentage. 4T1 cells were spread in 6-well plates and cultured overnight. The original medium was changed to PBS with four different pH values and 1.11 MBq of Fe_3O_4-PEG-[^{68}Ga]-DOTA/pHLIP NPs or Fe_3O_4-PEG-[^{68}Ga]DOTA NPs were added to each well. The mixture was incubated at 4 °C for 1 h. After being washed twice with ice-cold PBS buffer, the plates were imaged using a micro-PET/CT imaging system (InviScan) to analyze cell-associated radioactivity.

4.8. In Vivo MRI. An MRI scan was performed using a BioSpec 70/20 USR MRI system (Burker, Germany). T_1-weighted fast spin-echo imaging was performed under the following parameters: field of view (FOV) = 50 × 50 mm; slice thickness = 1 mm; TR = 200 ms; TE = 2.90 ms; flip angle = 50°; imaging matrix = 256 × 256, and total scan time: 5 min for each mouse model. Mice were anesthetized by inhalation oxygen containing 2% isoflurane, and ECG was monitored to ensure the normal signs of the anesthetized mouse model during imaging. Fe_3O_4-PEG-DOTA/pHLIP NPs and Fe_3O_4-PEG-DOTA NPs were injected into 4T1 tumor-bearing mice (body temperature ∼36.5 °C) through the tail vein separately (300 μg of iron per mouse, 200 μL). T_1-weighted MR images were acquired in the coronal planes before and after injection at times of 5, 15, 30, 1, and 2 h. Then, the region of interest (ROI) was defined to determine the signal intensity of the tumor area or normal tissues of the thoracic cavity. Signal intensities in similar locations within the tumor center were measured in defined ROIs using software (Image J; U.S. National Institutes of Health).

4.9. Small-Animal PET/CT. Small-animal PET/CT images on female nude mice bearing 4T1 tumor xenografts were obtained using the micro-PET/CT imaging system (InviScan). The experiment was divided into four groups with three mice in each group. In two groups, 1.11 MBq (100 μL) of Fe_3O_4-PEG-[^{68}Ga]DOTA NPs or Fe_3O_4-PEG-[^{68}Ga]DOTA NPs were injected via percutaneous intratumoral injection, and in the other two groups, 3.7 MBq (30 μL) of Fe_3O_4-PEG-[^{68}Ga]DOTA/pHLIP NPs or Fe_3O_4-PEG-[^{68}Ga]DOTA NPs were injected via the tail vein. Mice (body temperature ∼36.5 °C) were anesthetized by inhalation of 2% isoflurane (RWD Life Science, Shanghai) and imaged at 15, 48, and 75 min after injection. PET and CT fusion images were obtained using the automatic fusion function of the Nucline 2.0 program (InviScan).

Quantitative data were expressed as the mean ± SD. Means were compared using Student's t-test with Prism 8.0 (GraphPad Software, Inc.).

■ ASSOCIATED CONTENT

Supporting Information

The Supporting Information is available free of charge at https://pubs.acs.org/doi/10.1021/acsomega.1c05815.

Synthesis process of Fe_3O_4 NPs; magnetization curves of Fe_3O_4 NPs; FTIR spectra of NH_2-PEG-pHLIP and NH_2-PEG-DOTA; ^{1}H NMR spectra of the reactant and

https://doi.org/10.1021/acsomega.1c05815
ACS Omega 2022, 7, 3442−3451

the product; size distribution of Fe_3O_4 NPs with Gaussian fitting; TEM imaging and SAED of Fe_3O_4 NPs, Fe_3O_4-PEG-DOTA NPs, and Fe_3O_4-PEG-DOTA/pHLIP NPs; phantom image acquired from T_1/T_2-weighted MRI scans and the plot of the relaxation rates for Fe_3O_4-PEG-DOTA NPs at different Fe concentrations; T_1-weighted MR imaging of Fe_3O_4-PEG-DOTA and Fe_3O_4-PEG-DOTA/pHLIP NPs at different Fe concentrations; cytotoxicity of 4T1 cells treated with Fe_3O_4-PEG-DOTA NPs and Fe_3O_4-PEG-DOTA/pHLIP NPs; mean signal of in vitro tumor cellular uptake in different pH values; and PET/CT imaging after intravenous injection of probes (PDF)

AUTHOR INFORMATION

Corresponding Authors

Weina He − *Medical Chemistry and Bioinformatics Center, College of Basic Medical Sciences, Shanghai Jiao Tong University School of Medicine, Shanghai 200025, China*; orcid.org/0000-0003-1438-1871; Email: hewn0319@sjtu.edu.cn

Jianhua Liu − *Medical Chemistry and Bioinformatics Center, College of Basic Medical Sciences, Shanghai Jiao Tong University School of Medicine, Shanghai 200025, China*; Email: jhliu7912@sjtu.edu.cn

Qingqing Huang − *Shanghai Key Laboratory of Molecular Imaging, Shanghai University of Medicine and Health Sciences, Shanghai 201318, China*; Email: qingqinghuang80@gmail.com

Authors

Xiuyan Wei − *Medical Chemistry and Bioinformatics Center, College of Basic Medical Sciences, Shanghai Jiao Tong University School of Medicine, Shanghai 200025, China*

Haitao Zhao − *Department of Nuclear Medicine, Institute of Clinical Nuclear Medicine, Renji Hospital, School of Medicine, Shanghai Jiao Tong University, Shanghai 200127, China*

Gang Huang − *Shanghai Key Laboratory of Molecular Imaging, Shanghai University of Medicine and Health Sciences, Shanghai 201318, China*

Complete contact information is available at: https://pubs.acs.org/10.1021/acsomega.1c05815

Author Contributions

[‖]X.W. and H.Z. These authors contributed equally to this work. W.H. and J.L. conceived and designed the experiments; X.W. performed the chemical synthesis experiments; H.Z. performed the PET imaging test; X.W. analyzed the data; G.H. and Q.H. provided advice for the MRI analysis; X.W. and H.Z. wrote the paper; and W.H., J.L., and Q.H. provided essential edits to the paper. All authors have given approval to the final version of the manuscript.

Notes

The authors declare no competing financial interest.

ACKNOWLEDGMENTS

This research was financially supported by the National Natural Science Foundation of China (21504104 and 81671736), Shanghai Municipal Health Commission (2017YQ080), Shanghai Municipal Education Commission (16GC14), Construction Project of Shanghai Key Laboratory of Molecular Imaging (18DZ2260400), the Key Program of National Natural Science Foundation of China (81830052), and Frontier Research Youth Support Project of Shanghai Jiao Tong University School of Basic Medicine (YCTSQN2021001).

REFERENCES

(1) Kalinski, P. Tumor Immune Microenvironment in Cancer Progression and Cancer Therapy. *Adv. Exp. Med. Biol.* **2017**, *1036*, 236−239.

(2) Lebelo, M. T.; Joubert, A. M.; Visagie, M. H. Warburg effect and its role in tumourigenesis. *Arch. Pharm. Res.* **2019**, *42*, 833−847.

(3) Halcrow, P.; Khan, N.; Datta, G.; Ohm, J. E.; Chen, X.; Geiger, J. D. Importance of measuring endolysosome, cytosolic, and extracellular pH in understanding the pathogenesis of and possible treatments for glioblastoma multiforme. *Cancer. Rep.* **2019**, *2*, No. e1193.

(4) Deacon, J.; Engelman, D. M.; Barrera, F. N. Targeting acidity in diseased tissues: mechanism and applications of the membrane-inserting peptide, pHLIP. *Arch. Biochem. Biophys.* **2015**, *565*, 40−48.

(5) Svoronos, A. A.; Engelman, D. M. Pharmacokinetic modeling reveals parameters that govern tumor targeting and delivery by a pH-Low Insertion Peptide (pHLIP). *Proc. Natl. Acad. Sci. U.S.A.* **2021**, *118*, No. e2016605118.

(6) Reshetnyak, Y. K.; Andreev, O. A.; Lehnert, U.; Engelman, D. M. Translocation of molecules into cells by pH-dependent insertion of a transmembrane helix. *Proc. Natl. Acad. Sci. U.S.A.* **2006**, *103*, 6460−6465.

(7) Weerakkody, D.; Moshnikova, A.; Thakur, M. S.; Moshnikova, V.; Daniels, J.; Engelman, D. M.; Andreev, O. A.; Reshetnyak, Y. K. Family of pH (low) insertion peptides for tumor targeting. *Proc. Natl. Acad. Sci. U.S.A.* **2013**, *110*, 5834−5839.

(8) Wyatt, L. C.; Moshnikova, A.; Crawford, T.; Engelman, D. M.; Andreev, O. A.; Reshetnyak, Y. K. Peptides of pHLIP family for targeted intracellular and extracellular delivery of cargo molecules to tumors. *Proc. Natl. Acad. Sci. U.S.A.* **2018**, *115*, E2811−E2818.

(9) Demoin, D. W.; Wyatt, L. C.; Edwards, K. J.; Abdel-Atti, D.; Sarparanta, M.; Pourat, J.; Longo, V. A.; Carlin, S. D.; Engelman, D. M.; Andreev, O. A.; Reshetnyak, Y. K.; Viola-Villegas, N.; Lewis, J. S. PET Imaging of Extracellular pH in Tumors with (64)Cu- and (18)F-Labeled pHLIP Peptides: A Structure-Activity Optimization Study. *Bioconjugate Chem.* **2016**, *27*, 2014−2023.

(10) Wyatt, L. C.; Lewis, J. S.; Andreev, O. A.; Reshetnyak, Y. K.; Engelman, D. M. Applications of pHLIP Technology for Cancer Imaging and Therapy. *Trends Biotechnol.* **2017**, *35*, 653−664.

(11) Crawford, T.; Moshnikova, A.; Roles, S.; Weerakkody, D.; DuPont, M.; Carter, L. M.; Shen, J.; Engelman, D. M.; Lewis, J. S.; Andreev, O. A.; Reshetnyak, Y. K. pHLIP ICG for delineation of tumors and blood flow during fluorescence-guided surgery. *Sci. Rep.* **2020**, *10*, No. 18356.

(12) Demin, A. M.; Pershina, A. G.; Minin, A. S.; Brikunova, O. Y.; Murzakaev, A. M.; Perekucha, N. A.; Romashchenko, A. V.; Shevelev, O. B.; Uimin, M. A.; Byzov, I. V.; Malkeyeva, D.; Kiseleva, E.; Efimova, L. V.; Vtorushin, S. V.; Ogorodova, L. M.; Krasnov, V. P. Smart Design of a pH-Responsive System Based on pHLIP-Modified Magnetite Nanoparticles for Tumor MRI. *ACS Appl. Mater. Interfaces* **2021**, *13*, 36800−36815.

(13) Dharmaratne, N. U.; Kaplan, A. R.; Glazer, P. M. Targeting the Hypoxic and Acidic Tumor Microenvironment with pH-Sensitive Peptides. *Cells* **2021**, *10*, 541−554.

(14) Lee, D. E.; Koo, H.; Sun, I. C.; Ryu, J. H.; Kim, K.; Kwon, I. C. Multifunctional nanoparticles for multimodal imaging and theragnosis. *Chem. Soc. Rev.* **2012**, *41*, 2656−2672.

(15) Cheon, J.; LEE, J. H. Synergistically Integrated Nanoparticles as Multimodal Probes for Nanobiotechnology. *Acc. Chem. Res.* **2008**, *41*, 1630−1640.

(16) Decazes, P.; Hinault, P.; Veresezan, O.; Thureau, S.; Gouel, P.; Vera, P. Trimodality PET/CT/MRI and Radiotherapy: A Mini-Review. *Front. Oncol.* **2020**, *10*, No. 614008.
(17) Shi, S.; Chen, F.; Goel, S.; Graves, S. A.; Luo, H.; Theuer, C. P.; Engle, J. W.; Cai, W. In Vivo Tumor-Targeted Dual-Modality PET/Optical Imaging with a Yolk/Shell-Structured Silica Nanosystem. *Nano-Micro. Lett.* **2018**, *10*, 65.
(18) Fang, H.; Li, M.; Liu, Q.; Gai, Y.; Yuan, L.; Wang, S.; Zhang, X.; Ye, M.; Zhang, Y.; Gao, M. Ultra-sensitive Nanoprobe Modified with Tumor Cell Membrane for UCL/MRI/PET Multimodality Precise Imaging of Triple-Negative Breast Cancer. *Nano-Micro Lett.* **2020**, *12*, No. 62.
(19) Shah, S. N.; Huang, S. S. Hybrid PET/MR imaging: physics and technical considerations. *Abdom. Imaging* **2015**, *40*, 1358−1365.
(20) Drzezga, A.; Souvatzoglou, M.; Eiber, M.; Beer, A. J.; Furst, S.; Martinez-Moller, A.; Nekolla, S. G.; Ziegler, S.; Ganter, C.; Rummeny, E. J.; Schwaiger, M. First clinical experience with integrated whole-body PET/MR: comparison to PET/CT in patients with oncologic diagnoses. *J. Nucl. Med.* **2012**, *53*, 845−855.
(21) Cai, H.; Xiang, Y.; Zeng, Y.; Lia, Z.; Zheng, X.; Luo, Q.; Zhu, H.; Gong, Q.; Gua, Z.; Liu, Y.; Zhang, H.; Luo, K. Cathepsin B-responsive and gadolinium-labeled branched glycopolymer-PTX conjugate-derived nanotheranostics for cancer treatment. *Acta Pharm. Sin. B* **2021**, *11*, 544−559.
(22) Cai, H.; Dai, X.; Wang, X.; Tan, P.; Gu, L.; Luo, Q.; Zheng, X.; Li, Z.; Zhu, H.; Zhang, H.; Gu, Z.; Gong, Q.; Luo, K. A nanostrategy for efficient imaging-guided antitumor therapy through a stimuli-responsive branched polymeric prodrug. *Adv. Sci.* **2020**, *7*, No. 1903243.
(23) Guo, S.; Xiao, X.; Wang, X.; Luo, Q.; Zhu, H.; Zhang, H.; Li, H.; Gong, Q.; Luo, K. Reductive microenvironment responsive gadolinium-based polymers as potential safe MRI contrast agents. *Biomater. Sci.* **2019**, *7*, 1919−1932.
(24) Bouziotis, P.; Psimadas, D.; Tsotakos, T.; Stamopoulos, D.; Tsoukalas, C. Radiolabeled Iron Oxide Nanoparticles As Dual-Modality SPECT/MRI and PET/MRI Agents. *Curr. Top. Med. Chem.* **2013**, *12*, 2694−2702.
(25) Ehlerding, E. B.; Grodzinski, P.; Cai, W.; Liu, C. H. Big Potential from Small Agents: Nanoparticles for Imaging-Based Companion Diagnostics. *ACS Nano* **2018**, *12*, 2106−2121.
(26) Ali, Z.; Abbasi, A. Z.; Zhang, F.; Arosio, P.; Lascialfari, A.; Casula, M. F.; Wenk, A.; Kreyling, W.; Plapper, R.; Seidel, M.; Niessner, R.; Knoll, J.; Seubert, A.; Parak, W. J. Multifunctional nanoparticles for dual imaging. *Anal. Chem.* **2011**, *83*, 2877−2882.
(27) Dadfar, S. M.; Roemhild, K.; Drude, N. I.; von Stillfried, S.; Knuchel, R.; Kiessling, F.; Lammers, T. Iron oxide nanoparticles: Diagnostic, therapeutic and theranostic applications. *Adv. Drug Delivery Rev.* **2019**, *138*, 302−325.
(28) Shin, T. H.; Choi, Y.; Kim, S.; Cheon, J. Recent advances in magnetic nanoparticle-based multi-modal imaging. *Chem. Soc. Rev.* **2015**, *44*, 4501−4516.
(29) Javed, Y.; Akhtar, K.; Anwar, H.; Jamil, Y. MRI based on iron oxide nanoparticles contrast agents: effect of oxidation state and architecture. *J. Nanopart. Res.* **2017**, *19*, No. 366.
(30) Shen, Z.; Chen, T.; Ma, X.; Ren, W.; Zhou, Z.; Zhu, G.; Zhang, A.; Liu, Y.; Song, J.; Li, Z.; Ruan, H.; Fan, W.; Lin, L.; Munasinghe, J.; Chen, X.; Wu, A. Multifunctional Theranostic Nanoparticles Based on Exceedingly Small Magnetic Iron Oxide Nanoparticles for T1-Weighted Magnetic Resonance Imaging and Chemotherapy. *ACS Nano* **2017**, *11*, 10992−11004.
(31) Kim, B. H.; Lee, N.; Kim, H.; An, K.; Park, Y. I.; Choi, Y.; Shin, K.; Lee, Y.; Kwon, S. G.; Na, H. B.; Park, J. G.; Ahn, T. Y.; Kim, Y. W.; Moon, W. K.; Choi, S. H.; Hyeon, T. Large-scale synthesis of uniform and extremely small-sized iron oxide nanoparticles for high-resolution T1 magnetic resonance imaging contrast agents. *J. Am. Chem. Soc.* **2011**, *133*, 12624−12631.
(32) Wang, L.; Huang, J.; Chen, H.; Wu, H.; Xu, Y.; Li, Y.; Yi, H.; Wang, Y. A.; Yang, L.; Mao, H. Exerting Enhanced Permeability and Retention Effect Driven Delivery by Ultrafine Iron Oxide Nanoparticles with T1-T2 Switchable Magnetic Resonance Imaging Contrast. *ACS Nano* **2017**, *11*, 4582−4592.
(33) Garcia, J.; Tang, T.; Louie, A. Y. Nanoparticle-based multimodal PET/MRI probes. *Nanomedicine* **2015**, *10*, 1343−1359.
(34) Rees, P.; Wills, J. W.; Brown, M. R.; Barnes, C. M.; Summers, H. D. The origin of heterogeneous nanoparticle uptake by cells. *Nat. Commun.* **2019**, *10*, No. 2341.
(35) Blocker, S. J.; Shields, A. F. Imaging of nanoparticle distribution to assess treatments that alter delivery. *Mol. Imaging Biol.* **2018**, *20*, 340−351.
(36) Luo, Y.; Yang, J.; Yan, Y.; Li, J.; Shen, M.; Zhang, G.; Mignani, S.; Shi, X. RGD-functionalized ultrasmall iron oxide nanoparticles for targeted T(1)-weighted MR imaging of gliomas. *Nanoscale* **2015**, *7*, 14538−14546.
(37) Yang, Q.; Jones, S. W.; Parker, C. L.; Zamboni, W. C.; Bear, J. E.; Lai, S. K. Evading immune cell uptake and clearance requires PEG grafting at densities substantially exceeding the minimum for brush conformation. *Mol. Pharmceutics* **2014**, *11*, 1250−1258.
(38) Suk, J. S.; Xu, Q.; Kim, N.; Hanes, J.; Ensign, L. M. PEGylation as a strategy for improving nanoparticle-based drug and gene delivery. *Adv. Drug Delivery Rev.* **2016**, *99*, 28−51.
(39) Wang, C.; Cheng, L.; Liu, Y.; Wang, X.; Ma, X.; Deng, Z.; Li, Y.; Liu, Z. Imaging-Guided pH-Sensitive Photodynamic Therapy Using Charge Reversible Upconversion Nanoparticles under Near-Infrared Light. *Adv. Funct. Mater.* **2013**, *23*, 3077−3086.
(40) Böhmer, V. I.; Szymanski, W.; Feringa, B. L.; Elsinga, P. H. Multivalent Probes in Molecular Imaging: Reality or Future? *Trends Mol. Med.* **2021**, *27*, 379−393.
(41) Ferreira, C. L.; Lamsa, E.; Woods, M.; Duan, Y.; Fernando, P.; Bensimon, C.; Kordos, M.; Guenther, K.; Jurek, P.; Kiefer, G. E. Evaluation of Bifunctional Chelates for the Development of Gallium-Based Radiopharmaceuticals. *Bioconjugate Chem.* **2010**, *21*, 531−536.

https://doi.org/10.1021/acsomega.1c05815
ACS Omega 2022, 7, 3442−3451